Environmental
Science
Nano

ROYAL SOCIETY
OF CHEMISTRY

PAPER

Cite this: *Environ. Sci.: Nano*, 2025, **12**, 1249

Unveiling the micro-mechanism of H_2O_2 activation and the selective regulation strategy over single-atom catalysts†

Zhengyang Gao,[ab] Yuanzheng Qu,[ab] Chu Wang,[ab] Ruiyang Shi,[ab] Yixiao Sun,[ab] Qingqi Yan,[ab] Chenliang Ye *[ab] and Weijie Yang *[ab]

H_2O_2 is an important green oxidant, and activation of H_2O_2 is the key process determining its efficiency in removing environmental pollutants. However, due to complex catalytic sites and diverse active free radical products, the micro-mechanism of H_2O_2 activation and the selective regulation strategy are still ambiguous. Herein, single-atom catalysts (SACs) are selected as the model catalysts to investigate this fundamental mechanism. With a single active site, it is more beneficial to explain the mechanism. In this work, the differences in active free radical products (OH, ·OOH, $^1O_2$) of H_2O_2 over three SACs (Fe, Co, Cu) and intrinsic selective regulation strategies are elucidated based on electron paramagnetic resonance (EPR) and density functional theory (DFT) calculation. EPR testing suggests that Co-SAC has the highest production of ·OH radicals, while Cu-SAC surpasses the other two catalysts in generating both ·OOH and $^1O_2$ radicals. DFT calculations indicate that among the SACs, the lowest barrier of ·OH radical formation is Co-SAC (0.54 eV), while Cu-SAC demonstrates a notably lower energy barrier for ·OOH formation (0.26 eV) and $^1O_2$ generation (0.51 eV), which is consistent with the EPR experimental results. More importantly, our work reveals that there is a linear relationship between charge transfer and the energy barrier of free radical generation. When the charge transfer amount is greater than 1.02, it is more inclined to promote the generation of ·OOH, and it will generate $^1O_2$ free radicals when the charge transfer amount is smaller than 1.02. This work provides a predictive mechanism for SACs to selectively regulate the active free radical products, which is of great significance for developing green environmental protection technologies based on H_2O_2.

Received 26th October 2024,
Accepted 20th December 2024

DOI: 10.1039/d4en01005a

rsc.li/es-nano

Environmental significance

The activation process of H_2O_2 is a crucial factor for the efficient treatment of pollutants. However, the degradation rate of pollutants remains low due to the generation of various reactive oxygen species, thereby increasing the economic cost. In this paper, we discuss the energy barriers of generating several distinct free radicals during the activation of H_2O_2. By analyzing the electronic structure of single-atom catalysts in nanomaterials, the crucial factors governing the production of free radicals are uncovered. The accurate generation of free radicals is controlled. This study offers a predictive mechanism for the targeted generation of free radical products and reduces unnecessary free radical generation in the activation process, which is of great significance for the development of efficient and green environmental protection technology based on H_2O_2.

1 Introduction

Advanced oxidation processes (AOPs), as novel and comprehensive multi-pollutant elimination technologies, have demonstrated significant potential for development.[1–4] H_2O_2 is a green oxidant with strong oxidizing capacity, which is an ideal source of reactive oxygen species (ROS).[5,6] Through catalytic activation, H_2O_2 generates various active radicals, including superoxide radicals ($\cdot O_2^-$), hydroxyl radicals (·OH), and singlet oxygen ($^1O_2$), facilitating the efficient removal of various pollutants and playing a pivotal role in effectively mitigating organic contaminants.[7,8] However, due to the uncontrolled free radical species generated by H_2O_2 decomposition and the high self-decomposition rate, the economic feasibility of the current application in pollutant removal is not ideal.[9,10] Therefore, improving and regulating the selectivity of H_2O_2 in catalytic activation processes is crucial for enhancing its economic feasibility and effectiveness in pollutant elimination.

Currently, nearly all chemical production processes rely heavily on catalysis.[11] A number of strategies have been

---

[a] *Department of Power Engineering, North China Electric Power University, Baoding 071003, Hebei, China. E-mail: chenliangye@ncepu.edu.cn, yangwj@ncepu.edu.cn*
[b] *Hebei Key Laboratory of Low Carbon and High-Efficiency Power Generation Technology, North China Electric Power University, Baoding 071003, Hebei, China*

† Electronic supplementary information (ESI) available. See DOI: **https://doi.org/10.1039/d4en01005a**

reported to stimulate H_2O_2 activation.[12] The catalysis of H_2O_2 is plagued by two primary issues: inadequate production of free radicals and low selectivity in their generation.[13,14] To address these challenges, researchers have devised and fabricated an array of catalysts, employing strategies such as surface etching, coordination structure modification, carrier change, and manipulation of active centers.[15–19] For instance, Xu[20] reported a Bi@Bi_2MoO_6 catalyst with a 001 crystal surface boosting $^1O_2$ production by 3.9 times compared to its counterpart with a 010 crystal surface. Luo[21] designed FeOF with Fe–F coordination enhancing ·OH generation. Furthermore, Liu[22] optimized electro-Fenton catalysts by anchoring Fe on TiO_2, exploring metal effects on catalytic efficacy. In advanced oxidation processes (AOPs), ·OH radicals play a dominant role,[23,24] and enhancing the selectivity of H_2O_2 activation is crucial for the efficient removal of contaminants. Although high selectivity can be achieved by regulatory catalysts, the intrinsic microscopic mechanism of catalyst activation of H_2O_2 is still unclear due to the complex and diverse structures and reaction sites of these catalysts. The preparation methods of catalysts are diverse; thus, it is particularly important to design and prepare high-performance catalysts reasonably.[25] Therefore, there is an urgent need to identify a single-site catalyst that can elucidate these mechanisms, providing theoretical support for improving the selectivity of target products in future research.

Single-atom catalysts (SACs), which integrate metal ions with organic ligands through coordination bonds, form a carbon-based architecture centered around individual metal atoms.[26–29] It possesses a high specific surface area and a large number of active sites.[30,31] Compared to traditional particulate catalysts, atomically dispersed catalysts demonstrate superior physicochemical properties due to their atomic-level controllability.[32] Furthermore, the structural design of single-atom catalysts is simpler, offering greater flexibility and convenience in terms of modulation. SACs have shown promise in environmental governance,[33] with iron-doped MoS_2 achieving high pollutant removal rates[34] and Cu-anchored g-C_3N_4 increasing active site exposure.[35] As a model catalyst, single atom catalysts not only demonstrate there potential in improving catalytic efficiency, but also provide an ideal platform for studying the complex interactions between reactants, intermediates, and products in catalytic reactions.[36] Theoretical work by Yang *et al.* analyzed H_2O_2 adsorption and activation on SACs containing transition metals, highlighting the advantages of Fe SACs in catalytic oxidation.[37–39] Zhang *et al.* studied H_2O_2 activation on Cu–FeS catalysts, revealing changes in energy barriers.[40] However, current strategies for regulating single atom catalysts mainly focused on their high atomic utilization. They overlooked the selective advantage of single active sites, which is crucial for reducing by-products. Therefore, understanding and revealing the intrinsic mechanism of H_2O_2 activation selectivity on SACs, along with predicting and optimizing their coordination structures, proved crucial for advancing H_2O_2 catalytic efficiency and single atom catalyst precision control strategies.

Herein, three types of single-atom catalysts (SACs) with Fe, Co, and Cu as active centers were synthesized. Electron paramagnetic resonance (EPR) spectroscopy was used to probe the types and quantities of active free radicals generated through H_2O_2 activation. Co-SAC produced the highest amount of ·OH, whereas Cu-SAC generated more ·OOH and $^1O_2$ compared to the other two catalysts. Then, combined with density functional theory (DFT) calculation, the whole process of H_2O_2 activation was studied in detail. The rate determining step energy barrier for the generation of ·OH by Co-SAC was the lowest, while Cu-SAC had the lowest energy barrier for the generation of ·OOH and $^1O_2$. This finding was consistent with the experimental results. Furthermore, there is a clear linear relationship between charge transfer and the energy barrier of free radical formation. When charge transfer exceeds 1.02, ·OOH free radical energy barrier is lower and easier to generate. On the other hand, if the charge transfer is lower than 1.02, $^1O_2$ radicals are more easily formed. This finding provides a theoretical basis for the strategy of precise regulation of free radical generation.

2 Methods

2.1 Experimental methods

2.1.1 Chemicals. The experimental chemicals in this research include zinc nitrate hexahydrate ($Zn(NO_3)_2·6H_2O$, Kermel, 99%), copper(II) nitrate trihydrate ($Cu(NO_3)_2·3H_2O$, Kermel, 99%), cobalt nitrate hexahydrate ($Co(NO_3)_2·6H_2O$, Kermel, 99%), iron(III) nitrate nonahydrate ($Fe(NO_3)_3·9H_2O$, Macklin, 99.9%), 2-methylimidazole ($C_4H_6N_2$, Macklin, 98%), methanol (MeOH, Kermel, 99%), *p*-phthalic acid (TPA, Macklin, 99%), *p*-benzoquinone (*p*BQ, Macklin, 97%), and isopropyl alcohol (IPA, Kermel, 99%). All aqueous solutions were prepared using deionized water with a resistivity of 18.2 $M\Omega\ cm^{-1}$.

2.1.2 Synthesis of SACs. SACs were synthesized by pyrolysis at high temperature using a zeolite imidazole skeleton (ZIF-8) as a precursor.[41–44] The synthesis diagram is shown in Fig. S1.† We show the preparation procedure of Fe-SAC as an example. $Zn(NO_3)_2·6H_2O$ (3.39 g), $Fe(NO_3)_3·9H_2O$ (100 mg) and 2-methylimidazole (3.93 g) were mixed and dissolved in methanol to prepare a solution, which was heated in an oil bath at 60 °C and stirred magnetically for 24 h to obtain the Fe-ZIF-8 precursor containing the doped metal. Then, the precipitate was collected and centrifuged with methanol solution 3 times, and dried for 12 h. The dried solid was ground into powder and pyrolyzed for 2 h in a 900 °C nitrogen atmosphere to obtain carbon-based monatomic catalyst Fe-SAC. Except for replacing $Fe(NO_3)_3·9H_2O$ (100 mg) with $Co(NO_3)_2·6H_2O$ (130 mg) or $Cu(NO_3)_2·3H_2O$ (120 mg), the synthesis procedures of Co-SAC and Cu-SAC are the same as that of Fe-SAC.

2.1.3 Characterization of SACs. The structure and morphology of the catalysts were analyzed by the following techniques. The size, morphology and microstructure of the catalysts were studied by scanning electron microscopy (ZEISS SIGMA50) and transmission electron microscopy (Talos F200S G2). The crystal structure of the catalysts was characterized by X-ray diffraction (XRD) (Smartlab-SE). Fe-SAC and Co-SAC used cobalt with a wavelength of 1.7889 Å as the radiation source, and Cu-SAC used copper with a wavelength of 1.5406 Å as the radiation source. X-ray absorption fine structure (XAFS) techniques, including X-ray absorption near-side structure (XANES) and extended X-ray absorption fine structure (EXAFS), were performed at the Institute of Physics of the Chinese Academy of Sciences for the analysis of Fe K edge, Co K edge and Cu K edge. Iron foil, Fe_3O_4, cobalt foil, Co_3O_4, copper foil, and CuO served as references. The obtained EXAFS data are extracted and processed in accordance with standard procedures using IFEFFIT software and Athena module. The metal content of the catalysts was determined using an inductively coupled plasma optical emission spectrometer (ICP) (Saimofei, ICAP RQ). The Brunauer–Emmett–Teller surface area, Barrett–Joyner–Halenda (BJH) porosity, pore volume and other surface properties of the materials were determined by nitrogen adsorption–desorption at 77 K with a 3H-2000PM2 instrument.

2.1.4 EPR experiment. Three SACs (Fe, Co and Cu) were each dissolved in 1 mL deionized water with 5 mg each, and mixed with ultrasonication for 30 s. At 25 °C, 120 μL of 3 mol L^{-1} H_2O_2 solution was added to the catalyst mixture. DMPO solution (100 mM) was added at 5, 10, and 15 minutes, shaken well, and loaded into a capillary tube to test the ·OH radical signal peak intensity.

In addition, the radical signal peak strength of ·OOH free radicals was tested by mixing methanol and DMPO solution. The radical signal peak strength of $^1O_2$ free radicals was tested with deionized water and TEMP solution.

2.2 Calculation methods

All DFT calculations were based on the Vienna *ab initio* simulation package (VASP),[45,46] using the projector augmented wave (PAW)[47] method and Perdew–Burke–Ernzerhof (PBE)[48] functional. The generalized gradient approximation (GGA)[47] method was utilized to calculate the correlation interactions. The DFT-D3 framework was used to correct the van der Waals interaction. A 5 × 5 graphene with a vacuum layer of 15 Å was used to simulate the vicinity of the active center of SACs.[49] A 2 × 2 × 1 centered *k*-point and a 450 eV energy cutoff were used to perform geometric optimization. For each atom, the constriction force was set to 0.02 eV $Å^{-1}$. Using a 4 × 4 × 1 *k*-point grid and an electronic self-consistent calculation threshold of 10^{-5} eV, reliable information about the electronic configuration and ground-state energy was obtained.[50] In this study, the influence of the three catalysts on the activation process of H_2O_2 was studied under the condition that ISPIN was set to 2 in the VASP INCAR file during calculation. The information on *k*-point and energy tests is shown in Fig. S2.† Using the Bader charge analytical approach, the analysis of the charges was carried out.[51] The basic steps of the transition state were obtained jointly by the climbing image nudged elastic band (CI-NEB) method and the improved dimer method (IDM).[52,53] A 0.05 eV $Å^{-1}$ adjustment was made to the necessary force convergence criteria. The minimum value of displacement constraint of ±0.02 Å and the transition state structure were verified by vibration frequency analysis. The calculation equations of adsorption energy, energy barrier, and charge density difference are provided in the ESI.†

3 Results and discussion

3.1 Characterization of the catalysts

Through pyrolysis of metal–organic framework (MOF) material ZIF-8, three carbon-based single atom catalysts, Fe-SAC, Co-SAC, and Cu-SAC, are synthesized. Based on ICP results, the loadings of Fe in Fe-SAC, Co in Co-SAC and Cu in Cu-SAC are 1.33%, 1.07%, and 0.98% respectively (Table S1†). The BET results demonstrated that the specific surface areas of Fe-SAC, Co-SAC, and Cu-SAC were 432.62 m^2 g^{-1}, 537.93 m^2 g^{-1}, and 349.02 m^2 g^{-1} respectively (Table S2†), and the pore size of the catalyst is mainly distributed within the mesoporous range (Fig. S3, Table S1†). The abundant pore structure and large specific surface area are conducive to the uniform dispersion of metal atoms on the carbon base.

Scanning electron microscopy (SEM) images of the three catalysts show that the surface morphology of the three catalysts is a regular dodecahedral cubic structure (Fig. S4a–c†), indicating that no significant morphological changes occurred after the addition of metals. Transmission electron microscopy (TEM) images indicate that all the three catalysts present a hexagonal shape, and no distinct metal particles are observable (Fig. 1a–c). Furthermore, imaging of the three catalysts through aberration-corrected high-angle annular dark-field scanning transmission electron microscopy (HAADF-STEM) reveals bright spots in the images that unequivocally demonstrate the atomic-scale dispersion of metal atoms (Fig. 1d–f). These observations provide compelling evidence for the successful construction of catalysts rich in single-atom active sites on the ZIF-8 support. X-ray diffraction (XRD) curves reveal that there exist two characteristic peaks of graphitic carbon, namely (002) and (101), at the range of 20–30° and 40–45° for both ZIF-8 and the three SACs (Fe, Co and Cu) after carbonization (Fig. S5†).

In addition, the electronic structure and coordination environment of the active metals were measured by X-ray absorption near edge structure (XANES) and extended X-ray absorption fine structure (EXAFS). In the Fe K edge, the absorption edge of Fe-SAC moves in a high-energy direction compared to the iron foil (Fig. S6a†), indicating that the valence of Fe species in Fe-SAC is higher than that of Fe foil, and the EXAFS profile of Fe-SAC shows a peak at ≈1.47 Å, which differs from the Fe–Fe bond (≈2.2 Å) and is attributed to the Fe–N bond (Fig. 2a). In the Co K edge, compared with Co foil, the absorption edge of Co-SAC moves in a high-energy direction

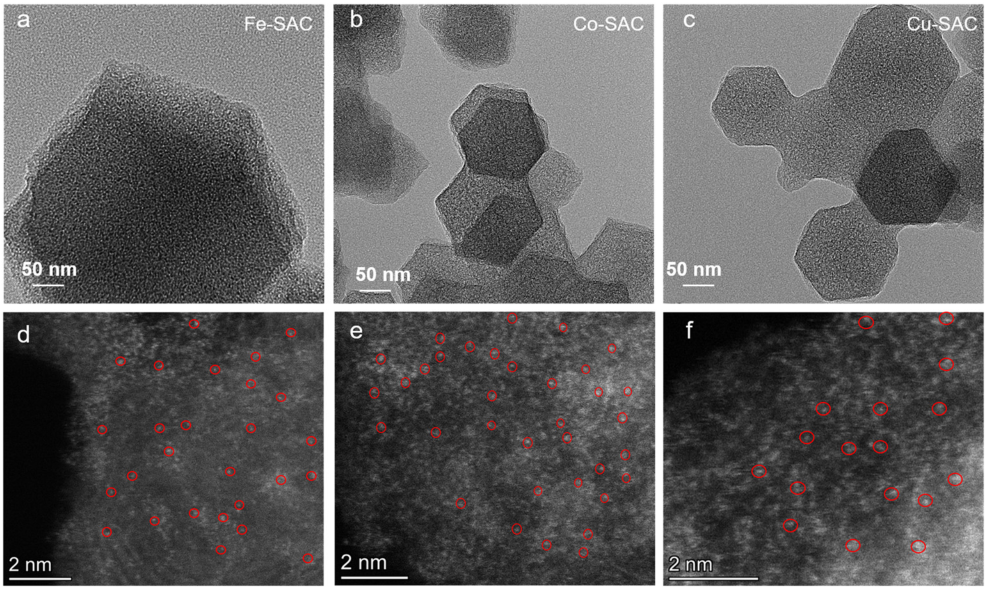

Fig. 1 TEM images of (a) Fe-SAC, (b) Co-SAC, and (c) Cu-SAC. HAADF-STEM images of (d) Fe-SAC, (e) Co-SAC, and (f) Cu-SAC.

(Fig. S6b†), and the EXAFS spectrum of Co-SAC has a main peak at ≈1.40 Å, corresponding to the Co–N scattering path without a Co–Co bond (≈2.20 Å) (Fig. 2b). In the Cu K edge, the absorption edge of Cu-SAC is higher than that of Cu foil, indicating that Cu has a high oxidation valence state in Cu-SAC (Fig. S6c†), and the EXAFS spectrum of Cu-SAC has a significant peak at ≈1.48 Å, which is different from the Cu–Cu bond (≈2.23 Å), and is attributed to the Cu–N bond (Fig. 2c). No metal–metal bond is found in the EXAFS spectra of the three catalysts, which suggests that the active metals are atomically dispersed on the supports. These results are also confirmed by wavelet transforms (WT). The maximum intensity values of the three single-atom catalysts significantly deviate from those of their corresponding metallic elements, ruling out the possibility of metal agglomeration in the samples (Fig. S7†). Through the fitting of EXAFS spectra, a precise coordination environment of the metal with N atoms is obtained (Fig. 2d–f, Table S3†), revealing a coordination with four N atoms.

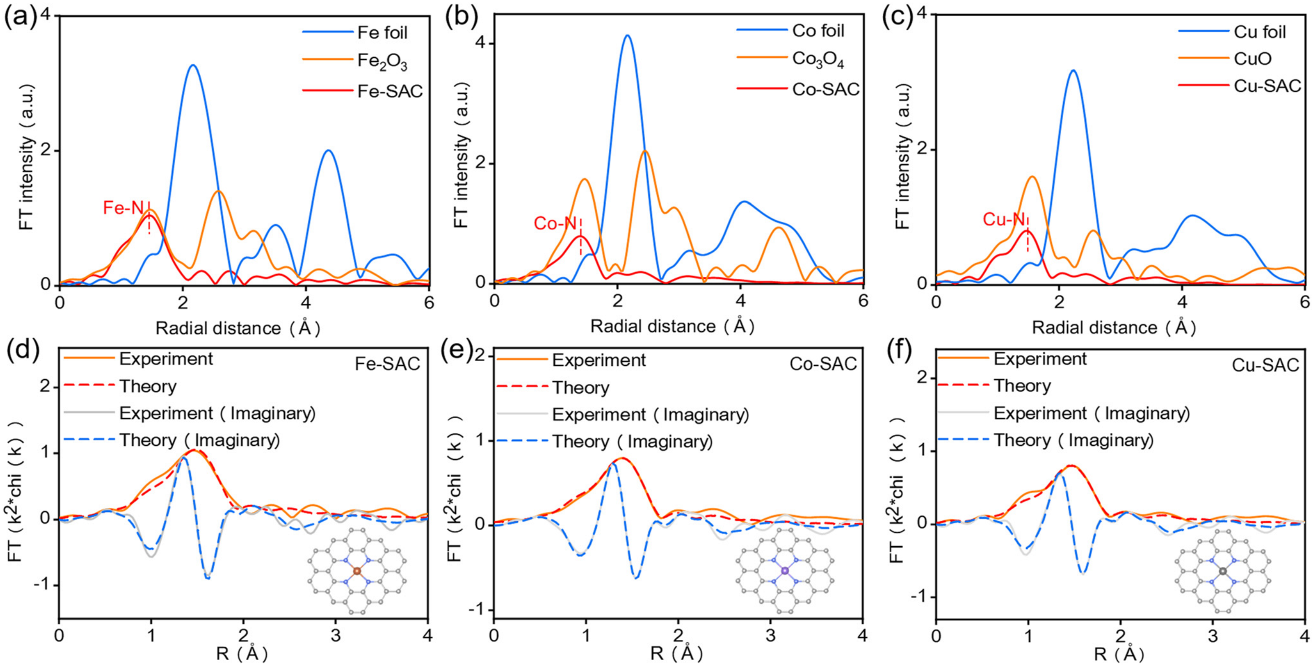

Fig. 2 EXAFS spectra of (a) Fe-SAC, (b) Co-SAC, and (c) Cu-SAC. EXAFS fitting of (d) Fe-SAC, (e) Co-SAC, and (f) Cu-SAC (inset: structural model; Fe red, Co purple, Cu cyan, N blue, C white).

3.2 H_2O_2 activation experiment

Electron paramagnetic resonance (EPR) technology can directly detect unpaired electrons in a sample, to obtain the types of free radicals contained in the sample.[54] Quantitative EPR measurements can provide the number of unpaired electron spins in a sample, allowing for the determination of the free radical content.[55] To study the catalytic performance of the single-atom catalysts prepared in this paper, experimental studies were conducted on the catalytic activation of H_2O_2 by all three catalysts. Based on quantitative EPR experiments, DMPO was used as the trapping agent of ·OH and $\cdot OOH/\cdot O_2^-$, and TEMP was used as the trapping agent of $^1O_2$ to detect the types of free radicals in the activation products of H_2O_2. The content of each product was compared through quantitative calculation of the spin-intensity peak of the free radical signals and related parameters. The concentration of H_2O_2 is 3 mol L^{-1} and the temperature is room temperature.

The results show that the detection results of H_2O_2 activation products catalyzed by the three carbon-based single-atom catalysts all contain the spectra of three kinds of products (Fig. 3). The spectrum diagram in Fig. 3a has 4 peaks, and the ratio of peaks is 1 : 2 : 2 : 1 in sequence, which is the characteristic peak of ·OH, indicating that ·OH is present in the activation product. In the spectra in Fig. 3b, the 3 peaks of equal height, with a ratio of 1 : 1 : 1, are characteristic peaks of $^1O_2$, indicating that the activation product contains $^1O_2$. There are four major and two minor peaks with a total of 6 peaks, which are the characteristic peaks of $\cdot OOH/\cdot O_2^-$, indicating that the activation product contains $\cdot OOH/\cdot O_2^-$ (Fig. 3c).

In addition, the contents of ·OH, $^1O_2$ and $\cdot OOH/\cdot O_2^-$ produced by the activation of H_2O_2 over the three catalysts were analyzed. For the convenience of problem analysis, the vertical axis represents the relative value of the free radical content produced by the catalyst, compared to the free radical content produced by the ZIF-8 precursor. This comparison

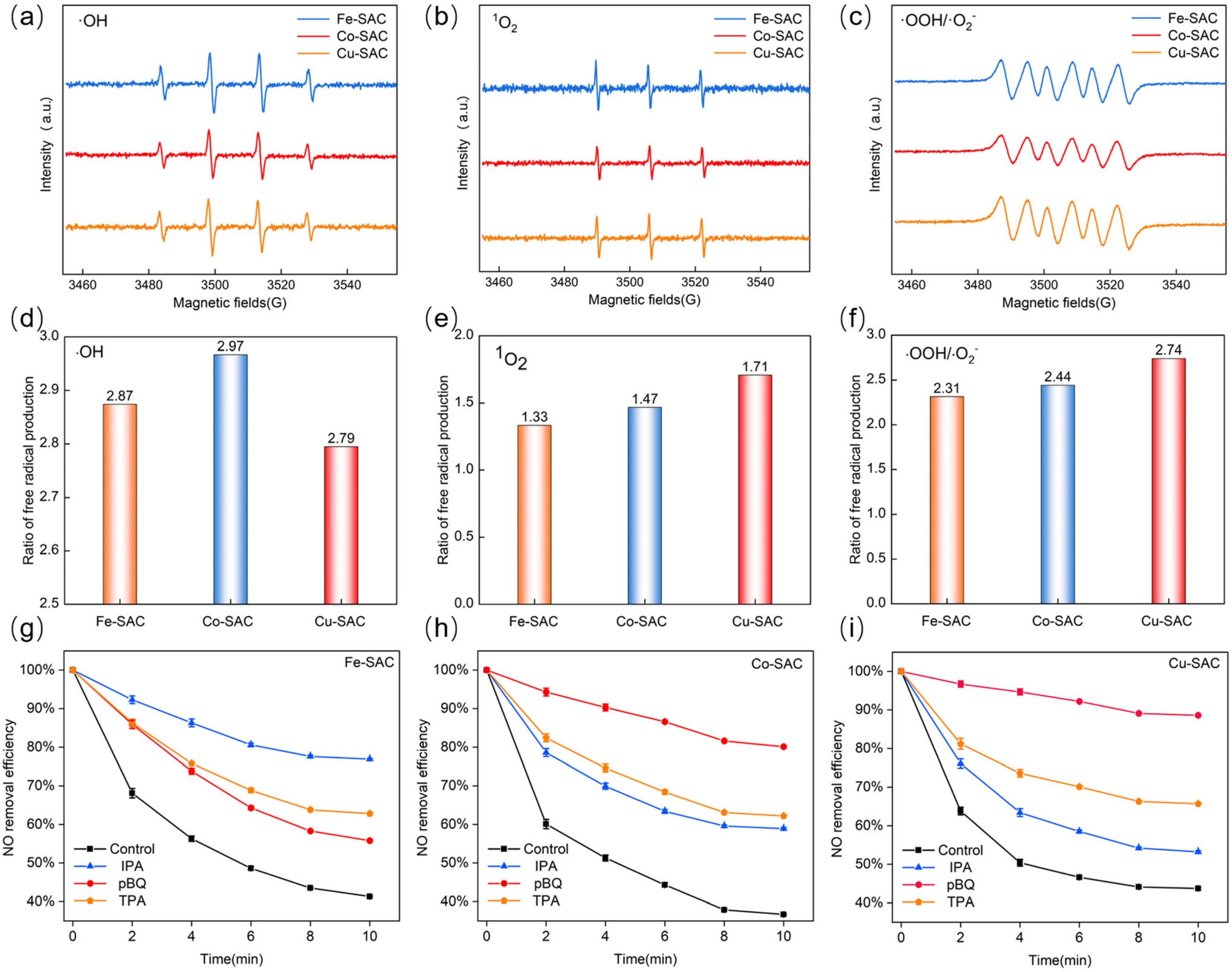

Fig. 3 EPR spectra of H_2O_2 activation to (a) ·OH, (b) $^1O_2$, and (c) $\cdot OOH/\cdot O_2^-$ by three kinds of SACs (Fe, Co and Cu; time: 10 min). The free radical content on the SACs of (d) ·OH, (e) $^1O_2$, and (f) $\cdot OOH/\cdot O_2^-$. The NO oxidation experiments with H_2O_2 were carried out on (g) Fe-SAC, (h) Co-SAC and (i) Cu-SAC.

helps to reduce experimental error. Among them, the Co-SAC catalyst has the highest ·OH content (Fig. 3d), suggesting that Co-SAC exhibits the best catalytic activity in catalyzing H_2O_2 to generate ·OH. Regarding the formation content of ·OOH/·O_2^-, the Cu-SAC catalyst is greater than the other catalysts (Fig. 3e), indicating that Cu-SAC has the best activity in catalyzing H_2O_2 activation for the formation of ·OOH/·O_2^-. Similarly, the Cu-SAC catalyst has a higher $^1O_2$ content compared to the other catalysts (Fig. 3f), demonstrating its superior catalytic activity for activating H_2O_2 to produce $^1O_2$.

This paper further adopts radical quenching experiments to investigate the specific contributions of radicals during the experimental process. The experiments primarily focus on the process of H_2O_2 oxidizing NO, using the removal efficiency for NO as the metric to deeply analyze the roles played by different radicals. Specifically, the experiments select IPA as the quencher for ·OH radicals, *p*BQ as the quencher for ·OOH radicals, and TPA as the quencher for $^1O_2$ radicals. For the experimental conditions, the concentration of H_2O_2 is set to 3 mol L^{-1}, and the experimental temperature is maintained at 140 °C.

Observing the results of the radical quenching experiments with Fe-SAC, we find that when ·OH radicals are quenched, the decrease in NO content is significantly reduced, and its reduction rate also slows down notably (Fig. 3g). This phenomenon strongly demonstrates that ·OH radicals play a dominant role during the experimental process. Similarly, in the experimental results of Co-SAC and Cu-SAC, we can also intuitively see that ·OOH radicals occupy a dominant position during the experimental process (Fig. 3h and i). Combining the results of EPR experiments and radical quenching experiments, whether from the comparison of the generation amounts of individual radicals under the action of different catalysts or from the effects of activating H_2O_2 to generate different radicals under the action of the same catalyst, it can be clearly revealed that during the activation process of H_2O_2, due to the role of the catalyst, there exists a significant selectivity towards radicals.

3.3 DFT calculation

3.3.1 Adsorption properties of H_2O_2 on TM_1–N_4–C. The adsorption energy (E_{ads}) and configuration of H_2O_2 on the three types of SAC surfaces have been calculated using DFT theory, considering both aqueous and anhydrous conditions (Fig. 4). In no water molecules, H_2O_2 dissociates into O atoms (*O) and H_2O on Fe-SAC, and the adsorption configuration on Co-SAC and Cu-SAC is free H_2O_2 molecules. After the introduction of H_2O clusters, the adsorption energy of H_2O_2 on the surface of the catalyst decreases, and the adsorption capacity of H_2O_2 is weakened. These results indicate that the hydrogen bonds of H_2O clusters have a certain effect on the adsorption of H_2O_2. The Bader charge transfer (Δq) of metal atoms (Fe, Co, Cu) during the adsorption of H_2O_2 on Fe-SAC, Co-SAC, and Cu-SAC has been calculated (Fig. 4). In the adsorption system of SACs and H_2O_2, the metal atom loses electrons and the O atom gains electrons. In addition, some H_2O molecules in the H_2O cluster are also involved in the charge transfer. Therefore, the activation of H_2O_2 gas will be affected by the water atmosphere, and the activation of H_2O_2 gas in the water environment is considered in the following calculations.

3.3.2 Reaction mechanism of H_2O_2 activation catalyzed by Fe-SAC. Based on the experimental results of H_2O_2 activation, the mechanism of Fe-SAC catalyzing the H_2O_2 activation path was analyzed by DFT theory (Fig. 5).

*H_2O_2 serves as the initial state (IS1) for the activation reaction. The reaction path step-1 has two sub-paths (Fig. 5a). One path involves the dissociation of H_2O_2 to produce *O and H_2O. The reaction energy barrier for this process is 1.24 eV. The reaction is exothermic, releasing 1.52 eV of heat (Fig. S8a†). The other sub-pathway involves the dissociation of H_2O_2 into two adsorbed *OH states, with an energy barrier of

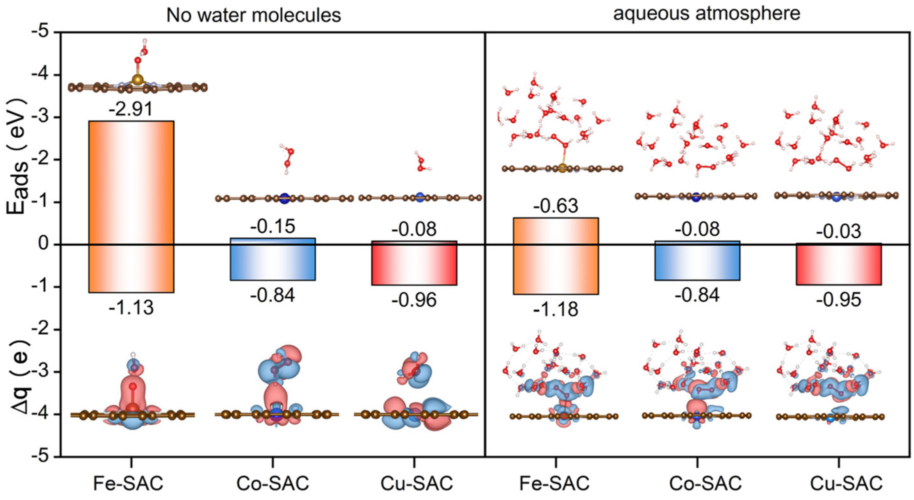

Fig. 4 Adsorption energy and electron density difference diagram and configuration of H_2O_2 on the three kinds of SACs (in the presence and absence of water, respectively; the blue areas are lost electrons, and the red areas are gained electrons). The brown, red, white, pink, yellow, dark blue, and blue spheres represent C, O, N, H, Fe, Co, and Cu, respectively.

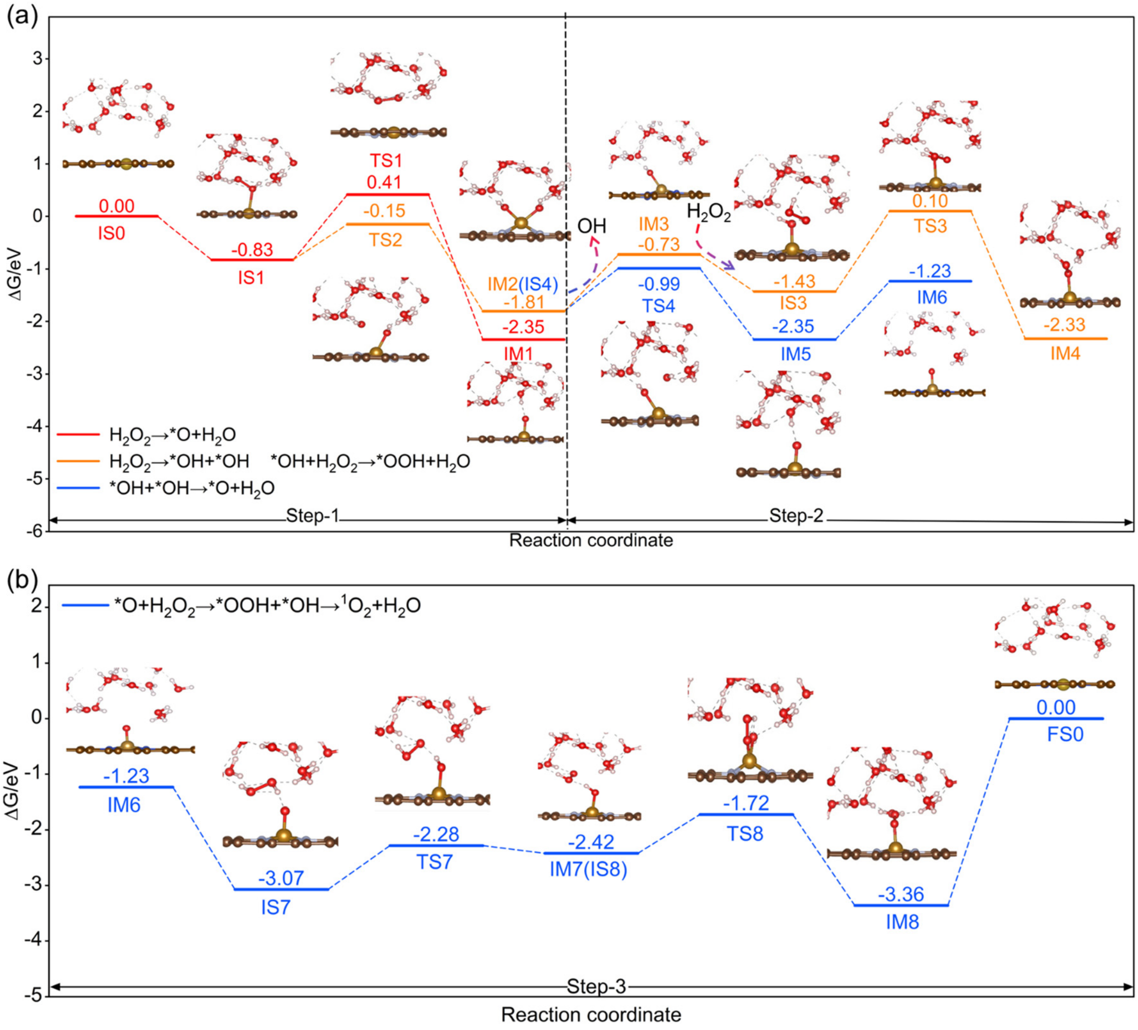

Fig. 5 Activation reaction network of H_2O_2 on Fe-SAC. (a) Step-1 and step-2. (b) Step-3. The brown, red, white, pink, and yellow spheres represent C, O, N, H, and Fe, respectively.

0.68 eV. It is an exothermic reaction, and the exothermic reaction is 0.98 eV (Fig. S8b†). In the two sub-paths of step-1, the reaction energy barrier of H_2O_2 dissociation into two adsorbed *OH state paths is 0.68 eV, which is much lower than the 1.24 eV of H_2O_2 dissociation to *O and H_2O. Consequently, the formation of 2*OH is the main reaction of step-1. *OH is an intermediate in step-2 of the subsequent activation reaction.

Step-2 can be divided into two paths (Fig. 5a). In one path, H_2O_2 reacts with *OH to produce *OOH and H_2O. The reaction energy barrier for this process is 1.53 eV, and it is an exothermic reaction with a heat release of 0.90 eV (Fig. S8c†). The other path introduces two *OH reactions to generate *O and H_2O with a reaction energy barrier of 0.82 eV and an exothermic reaction of 0.54 eV (Fig. S8d†). The energy barriers of these two pathways are 0.82 eV and 1.53 eV, respectively. The energy barriers for the activation of H_2O_2 into *O and H_2O are lower, so *O (IM 6) serves as an intermediate for subsequent activation steps. In step-3, H_2O_2 is introduced to react with *O to produce *OOH and *OH (Fig. 5b), and the reaction energy barrier is 0.79 eV. This reaction is endothermic, with an energy requirement of 0.65 eV for the endothermic process (Fig. S8e†). Then, *OH and *OOH continue to react under the action of Fe-SAC to produce H_2O and $^1O_2$ with a reaction energy barrier of 0.70 eV. The reaction is exothermic with a heat release of 0.94 eV (Fig. S8f†).

The catalytic process for H_2O_2 activation facilitated by Co-SAC is fundamentally similar to that of Fe-SAC (Fig. S9 and S10†). The energy barriers of ·OH, ·OOH and $^1O_2$ free radical formation are 0.54 eV, 0.26 eV and 0.58 eV, respectively.

3.3.3 Reaction mechanism of H_2O_2 activation catalyzed by Cu-SAC. Based on the experimental results of H_2O_2 activation, the mechanism of Cu-SAC catalyzing the H_2O_2 activation path was analyzed by DFT theory (Fig. 6).

The initial stage of the step-1 reaction is very similar to the initial catalytic mechanism employed by the first two catalysts (Fig. 6a). Here, we compare the reaction energy barriers of the two different pathways: the potential barrier for the formation of *O + H_2O is 1.10 eV, and the potential

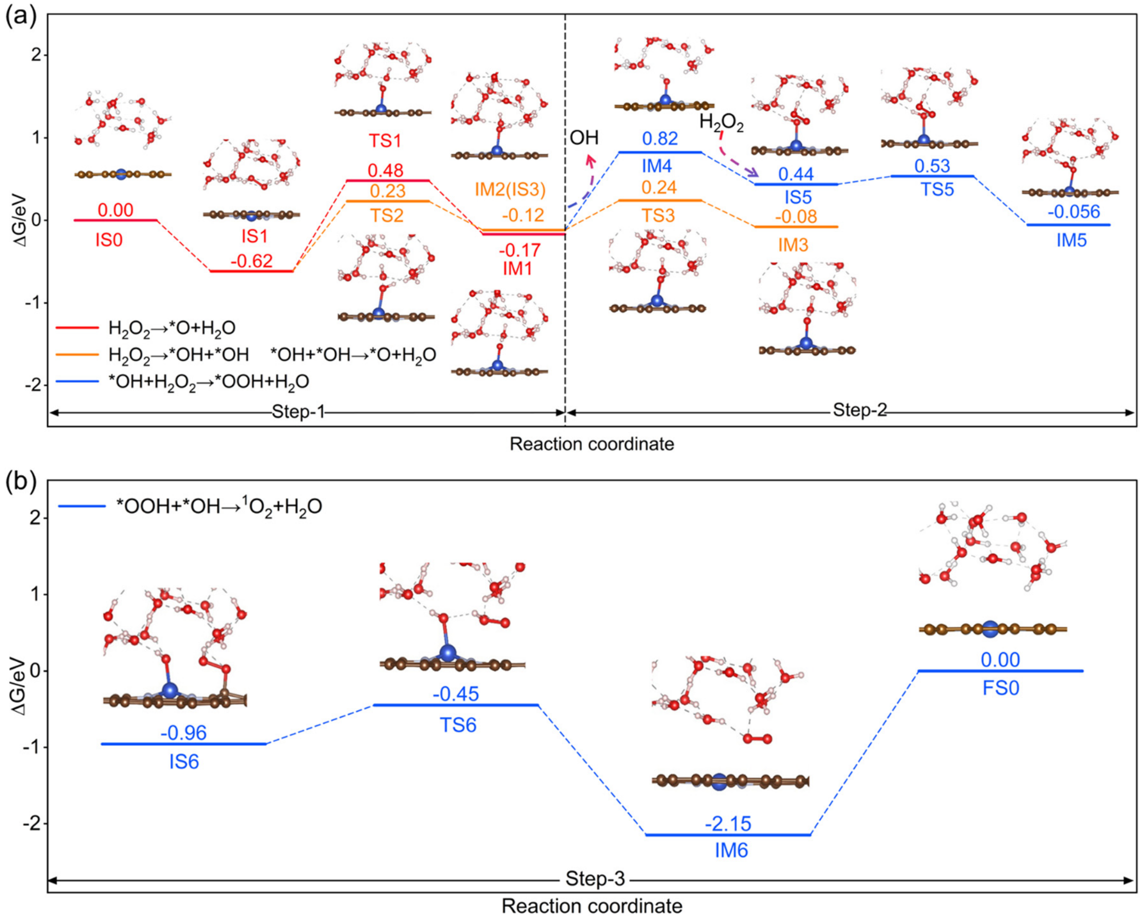

Fig. 6 Activation reaction network of H_2O_2 on Cu-SAC. (a) Step-1 and step-2. (b) Step-3. The brown, red, white, pink, and blue spheres represent C, O, N, H, and Cu, respectively.

barrier for the formation of *OH + *OH is lower at 0.85 eV. This indicates that the reaction of OH formation is more likely to occur. Therefore, in the step-1 reaction, it is mainly the dissociation of H_2O_2 into two *OH radicals. Subsequently, *OH acts as a key intermediate that facilitates the activation reaction in the subsequent step-2.

Path step-2 is also discussed in two cases (Fig. 6a). First, H_2O_2 is introduced to react with *OH to generate *OOH and H_2O, the reaction energy barrier is 0.10 eV, and the heat release is 0.49 eV (Fig. S11c†). In the other path, two *OH react to form *O and H_2O, with a reaction energy barrier of 1.53 eV and a heat release of 0.90 eV (Fig. S11d†). The energy barrier for the reaction of two ·OH radicals to produce *O and H_2O is greater than the energy barrier for the reaction of H_2O_2 with ·OH to produce *OOH and H_2O. Therefore, the main reaction in path step-2 is the reaction of H_2O_2 with ·OH to produce *OOH and H_2O. This step is different from the reaction of the previous two catalysts. In step-3, *OOH reacts with the free *OH on the surface of Cu–N_4–C to produce H_2O and $^1O_2$, with a reaction energy barrier of 0.51 eV and a heat release of 1.19 eV (Fig. 6b and S11e†).

3.3.4 Analysis of the three kinds of SACs and catalytic activity of H_2O_2. We found that the first step of H_2O_2 activation on the three kinds of SAC surfaces is to break the O–O bond and generate two hydroxyl radicals ·OH. Studies by other scholars have also shown that the decomposition of H_2O_2 on the surface of various catalysts is more inclined to break the O–O bond.[56,57] Through our exploration of the H_2O_2 activation mechanisms on three distinct catalysts, we have determined the crucial energy barriers associated with free radicals during catalyst activation (Fig. 7a). The energy barriers for the activation of H_2O_2 to ·OH, catalyzed by Fe-SAC, Co-SAC, and Cu-SAC, are 0.68 eV, 0.54 eV, and 0.85 eV, respectively. Similarly, for the generation of ·OOH, the energy barriers are 0.79 eV, 0.26 eV, and 0.10 eV when catalyzed by Fe-SAC, Co-SAC, and Cu-SAC, respectively. Lastly, for the activation of $^1O_2$, the corresponding energy barriers are 0.70 eV, 0.58 eV, and 0.51 eV for Fe-SAC, Co-SAC, and Cu-SAC, respectively. Co-SAC catalyzes H_2O_2 activation to produce ·OH with the lowest reaction energy barrier, while Cu-SAC catalyzes H_2O_2 activation to produce ·OOH and $^1O_2$ with the lowest reaction energy barrier. The results of theoretical calculation reveal the reaction mechanism of the macroscopic activation experiment at the microscopic level.

The adsorption energies and charge transfer of three different types of radicals adsorbed on various catalysts have

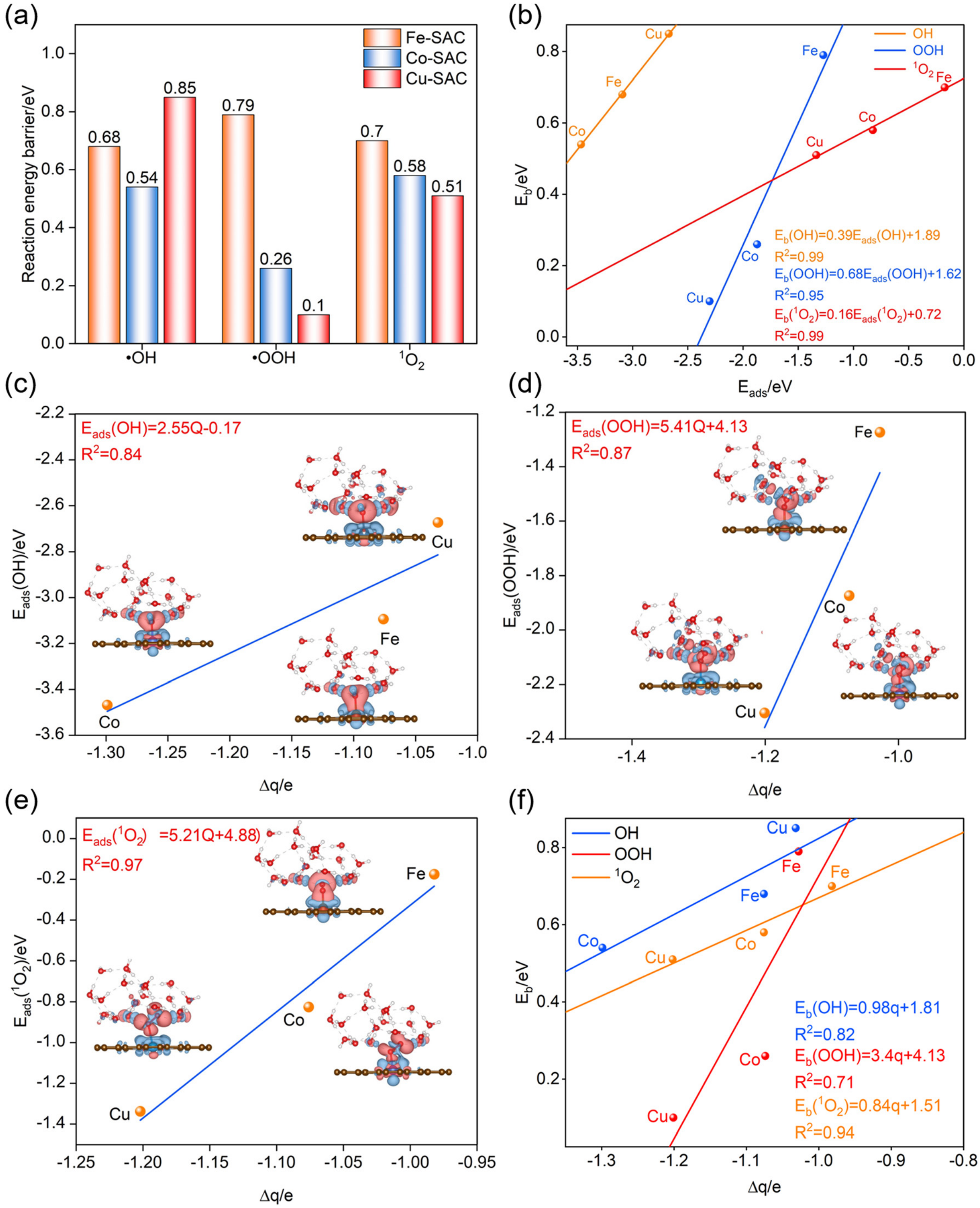

Fig. 7 (a) Three kinds of SACs (Fe, Co and Cu) catalyze the activation of H_2O_2 to generate the reaction energy barrier of each product. (b) Linear correlations of E_{ads} *vs.* E_b. (c) Linear correlations of E_{ads} (OH) *vs.* Bader charge. (d) Linear correlations of E_{ads} (OOH) *vs.* Bader charge. (e) Linear correlations of E_{ads} ($^1O_2$) *vs.* Bader charge. (f) Linear correlations of electric charge *vs.* E_b. The blue areas are lost electrons, and the red areas are gained electrons. The brown, red, white, pink, yellow, dark blue, and blue spheres represent C, O, N, H, Fe, Co, and Cu, respectively.

been calculated (Tables S4–S6†). The relationship between the adsorption energy and the formation energy barrier of three distinct types of free radicals on various catalysts is also examined. As illustrated in Fig. 7b, there is a positive correlation between the adsorption energy of these free radicals and their respective formation energy barriers. And the formation energy barrier decreases with the increase of adsorption energy. Furthermore, given the pivotal role of electron transfer in unraveling reaction mechanisms,[58,59] we delved into the interplay between charge transfer and radical adsorption energies. Electron acquisition is denoted by red markers, whereas electron loss is represented by blue markers (Fig. 7c–e).

Subsequently, we delved into the correlation between charge transfer and adsorption energy. A discernible linear correlation emerges between charge transfer and adsorption energy. Notably, Co-SAC demonstrated the highest levels of both charge transfer and adsorption energy during the formation of ·OH radicals. Conversely, Cu-SAC exhibited the highest charge transfer and adsorption energy during the formation of ·OOH and $^1O_2$ radicals. Intriguingly, we find a linear relationship between adsorption energy and the energy barrier, and furthermore, charge transfer is also linked to adsorption energy. These findings suggest that the magnitude of charge transfer can serve as an indicator for assessing the ease of radical generation. To further explore this, we systematically examined the relationship between the charge magnitude and the energy barrier dimensions. Our results revealed a pronounced positive correlation between these two factors. By analyzing the charge quantity, we gain insights into the influence of diverse catalysts on the production of free radicals (Fig. 7f). Specifically, when the charge falls below $-1.02e$, the ·OOH radical exhibits the lowest energy barrier, facilitating its generation as the most prevalent among the three considered free radicals. Conversely, when the charge exceeds $-1.02e$, the $^1O_2$ radical becomes the preferred species due to its minimized energy barrier of the rate-determining step, rendering it readily formable. This assessment of charge quantity enables predictive capabilities in determining the free radical generation profile during H_2O_2 activation catalyzed by various catalysts. It thereby facilitating targeted modulation and efficient remediation strategies for pollutants.

4 Conclusions

In summary, the micro-mechanism of H_2O_2 activation and the selective regulation strategy over single-atom catalysts were systematically studied from both experimental and theoretical investigations. First, three kinds of SACs (Fe, Co, and Cu) were synthesized and characterized through X-ray absorption fine structure. The EPR experiment showed that the catalysts that catalyzed the activation of H_2O_2 mainly produced three free radicals ·OH, ·OOH and $^1O_2$, among which Co-SAC produced the most ·OH radicals. The Cu-SAC catalyst produced more ·OOH and $^1O_2$ than the other two catalysts, indicating that H_2O_2 activation had different selectivity on different catalysts. Based on DFT calculation, the reaction mechanism of H_2O_2 activation catalyzed by the three catalysts was discussed. The energy barrier of the activation of H_2O_2 on the three catalysts to produce three different kinds of free radicals were calculated. Co-SAC exhibited the lowest energy barrier (0.68 eV) for generating ·OH radicals compared to the other two catalysts, whereas Cu-SAC demonstrated the lowest energy barriers for producing ·OOH (0.1 eV) and $^1O_2$ (0.51 eV) among the three catalysts. The calculated results are in good agreement with the experimental results. Subsequent analysis delved into the correlation between the electronic structure of the catalysts and the energy barriers for free radical formation, revealing a linear relationship between the electronic configuration and the formation energies of the free radicals. This finding enables the prediction of free radical formation based on the catalyst's electronic structure, offering a theoretical framework for future catalyst optimization. This study not only experimentally validates the selectivity of the catalysts towards H_2O_2 activation but also delves into the underlying activation mechanisms through DFT calculations, while proposing strategies for catalyst regulation. These findings pave the way for the efficient utilization of H_2O_2 in pollutant remediation, presenting a novel perspective for environmental remediation.

Data availability

Data are available upon request from the authors.

Author contributions

Zhengyang Gao: wrote the first draft of the thesis, corrected the writing of the manuscript, the structure construction of the paper, the relevant theoretical support, and clarified the research subject and ideas of the paper. Yuanzheng Qu: completed the revision of the thesis under the supervisor's guidance and completed the calculation of the thesis results and graphical plotting work. Chu Wang and Ruiyang Shi: provided the relevant research data for the thesis. Yixiao Sun: participated in the correction of the thesis manuscript. Qingqi Yan: participated in the paper data analysis. Chenliang Ye: provided corresponding theoretical support and research ideas. Weijie Yang: guided the manuscript writing process, participated in the revision of the manuscript, verified the thesis and carefully reviewed the results of each part of the paper.

Conflicts of interest

There are no conflicts to declare.

Acknowledgements

This work was funded by the National Natural Science Foundation of China (No. 52176104 and 52006073).

References

1 M. Priyadarshini, I. Das, M. M. Ghangrekar and L. Blaney, Advanced oxidation processes: Performance, advantages, and scale-up of emerging technologies, *J. Environ. Manage.*, 2022, **316**, 115295.

2 J. Mukherjee, B. K. Lodh, R. Sharma, N. Mahata, M. P. Shah, S. Mandal, S. Ghanta and B. Bhunia, Advanced oxidation process for the treatment of industrial wastewater: A review on strategies, mechanisms, bottlenecks and prospects, *Chemosphere*, 2023, **345**, 140473.

3 J. Ji, Z. Wang, Q. Xu, Q. Zhu and M. Xing, In situ H_2O_2 Generation and Corresponding Pollutant Removal Applications: A Review, *Chemistry*, 2023, **29**, e202203921.

4 B. Yuan, X. Z. Mao, Z. Wang, R. L. Hao and Y. Zhao, Radical-induced oxidation removal of multi-air-pollutant: A critical review, *J. Hazard. Mater.*, 2020, **383**, 121162.

5 Y. Xing, Z. Yao, W. Li, W. Wu, X. Lu, J. Tian, Z. Li, H. Hu and M. Wu, Fe/Fe_3C Boosts H_2O_2 Utilization for Methane Conversion Overwhelming O_2 Generation, *Angew. Chem., Int. Ed.*, 2021, **60**, 8889–8895.

6 X. Chen, J. Gao, W. He, H. Liu, M. Wu, M. Qi, L. Yang, F. Liu and R. Hao, Ce/W-MIL-88B(Fe) photo-Fenton material achieving synchronous arsenate uptake and nitrite resourcing: unexpected role of arsenate in boosting photo-Fenton activity, *Environ. Sci.: Nano*, 2024, **11**, 4266–4278.

7 B. Wang, Z. Song and L. Sun, A review: Comparison of multi-air-pollutant removal by advanced oxidation processes – Industrial implementation for catalytic oxidation processes, *Chem. Eng. J.*, 2021, **409**, 128136.

8 B. Yuan, Z. Qian, Q. Yu, R. Hao and Y. Zhao, Ultraviolet-induced nitric oxide removal using H_2O/O_2 catalyzed by Fe/TiO_2: Feasibility and prospect, *Fuel*, 2021, **290**, 120026.

9 Y. Zhao, B. Yuan, Y. Shen, R. Hao and S. Yang, Simultaneous removal of NO and SO_2 from flue gas using vaporized H_2O_2 catalyzed by nanoscale zero-valent iron, *Environ. Sci. Pollut. Res.*, 2018, **25**, 25526–25537.

10 R. Hao, Z. Ma, Z. Qian, Y. Gong, Z. Wang, Y. Luo, B. Yuan and Y. Zhao, New insight into the behavior and cost-effectiveness of different radicals in the removal of NO and Hg^0, *Chem. Eng. J.*, 2020, **385**, 123885.

11 K. Zhang, Y. Li, S. Yuan, L. Zhang and Q. Wang, Review of S-Scheme Heterojunction Photocatalyst for H_2O_2 Production, *Wuli Huaxue Xuebao*, 2023, **39**, 2212010.

12 L. Zhu, J. Ji, J. Liu, S. Mine, M. Matsuoka, J. Zhang and M. Xing, Designing 3D-MoS_2 Sponge as Excellent Cocatalysts in Advanced Oxidation Processes for Pollutant Control, *Angew. Chem., Int. Ed.*, 2020, **59**, 13968–13976.

13 B. Wu, Y. Xiong and Y. Ge, Simultaneous removal of SO_2 and NO from flue gas with OH from the catalytic decomposition of gas-phase H_2O_2 over solid-phase $Fe_2(SO_4)_3$, *Chem. Eng. J.*, 2018, **331**, 343–354.

14 X. Chen, Y. Li, W. Fu, S. Tian, Y. Yang, K. Yang, X. Xu and X. Zhang, Oriented generation of singlet oxygen in H_2O_2activation for water decontamination: regulation of oxygen vacancies over α-MnO_2 nanocatalysts, *Environ. Sci.: Nano*, 2023, **10**, 1428–1440.

15 X. Liu, Y. Liu, W. Yang, X. Feng and B. Wang, Controlled Modification of Axial Coordination for Transition-Metal Single-Atom Electrocatalyst, *Chemistry*, 2022, **28**, e202201471.

16 M. C. Zhang, K. X. Zhang, X. Ai, X. Liang, Q. Zhang, H. Chen and X. X. Zou, Theory-guided electrocatalyst engineering: From mechanism analysis to structural design, *Chin. J. Catal.*, 2022, **43**, 2987–3018.

17 R. Long, K. Mao, X. Ye, W. Yan, Y. Huang, J. Wang, Y. Fu, X. Wang, X. Wu, Y. Xie and Y. Xiong, Surface facet of palladium nanocrystals: a key parameter to the activation of molecular oxygen for organic catalysis and cancer treatment, *J. Am. Chem. Soc.*, 2013, **135**, 3200–3207.

18 B. Gong, C. Ku, H.-Q. Yu and P. H. L. Sit, Density Functional Theory Investigation into the Effects of Dissolved Organic Matter on H_2O_2 Activation over α-Fe_2O_3 (001) Surfaces, *J. Phys. Chem. C*, 2021, **125**, 8508–8517.

19 Z. Qian, Y. Guo, M. Luo, L. Yang, S. Liu, P. Qin, B. Yuan, F. Liu and R. Hao, Unveiling the activity difference cause and ring-opening reaction routes of typical radicals induced degradation of toluene, *J. Hazard. Mater.*, 2024, **471**, 134273.

20 X. Xu, N. Yang, P. Wang, S. Wang, Y. Xiang, X. Zhang, X. Ding and H. Chen, Highly Intensified Molecular Oxygen Activation on Bi@Bi_2MoO_6 via a Metallic Bi-Coordinated Facet-Dependent Effect, *ACS Appl. Mater. Interfaces*, 2020, **12**, 1867–1876.

21 D. Yu, L. Xu, K. Fu, X. Liu, S. Wang, M. Wu, W. Lu, C. Lv and J. Luo, Electronic structure modulation of iron sites with fluorine coordination enables ultra-effective H_2O_2 activation, *Nat. Commun.*, 2024, **15**, 2241.

22 X. Liu, G. Bi, Y. Fang, C. Wei, J. Song, Y.-X. Wang, X. Zheng, Q. Sun, Y. Wang, G. Wang and Y. Mu, Regulating Surface Dipole Moments of TiO_2 for the pH-Universal Cathodic Fenton-Like Process, *Environ. Sci. Technol.*, 2024, **58**, 9436–9445.

23 P. Jiang, T. Zhou, J. Bai, Y. Zhang, J. Li, C. Zhou and B. Zhou, Nitrogen-containing wastewater fuel cells for total nitrogen removal and energy recovery based on Cl*/ClO* oxidation of ammonia nitrogen, *Water Res.*, 2023, **235**, 119914.

24 L. Li, J. Bai, P. Jiang, Y. Zhang, T. Zhou, J. Wang, C. Zhou, J. Li and B. Zhou, Efficient H_2O_2 Electrosynthesis and Its Electro-Fenton Application for Refractory Organics Degradation, *Engineering*, 2023, **30**, 131–143.

25 Y. Wang, F. Ma, G. Zhang, J. Zhang, H. Zhao, Y. Dong and D. Wang, Precise synthesis of dual atom sites for electrocatalysis, *Nano Res.*, 2024, **17**, 9397–9427.

26 C. Gao, J. Low, R. Long, T. Kong, J. Zhu and Y. Xiong, Heterogeneous Single-Atom Photocatalysts: Fundamentals and Applications, *Chem. Rev.*, 2020, **120**, 12175–12216.

27 B. Qiao, A. Wang, X. Yang, L. F. Allard, Z. Jiang, Y. Cui, J. Liu, J. Li and T. Zhang, Single-atom catalysis of CO oxidation using Pt1/FeOx, *Nat. Chem.*, 2011, **3**, 634–641.

28 Y. Chen, R. Gao, S. Ji, H. Li, K. Tang, P. Jiang, H. Hu, Z. Zhang, H. Hao, Q. Qu, X. Liang, W. Chen, J. Dong, D. Wang and Y. Li, Atomic-Level Modulation of Electronic Density at Cobalt Single-Atom Sites Derived from Metal–Organic Frameworks: Enhanced Oxygen Reduction Performance, *Angew. Chem.*, 2020, **133**, 3249–3258.

29 E. Zhang, L. Tao, J. An, J. Zhang, L. Meng, X. Zheng, Y. Wang, N. Li, S. Du, J. Zhang, D. Wang and Y. Li, Engineering the Local Atomic Environments of Indium Single-Atom Catalysts for Efficient Electrochemical Production of Hydrogen Peroxide, *Angew. Chem., Int. Ed.*, 2022, **61**, e202117347.

30 H. He, H. H. Wang, J. Liu, X. Liu, W. Li and Y. Wang, Research Progress and Application of Single-Atom Catalysts: A Review, *Molecules*, 2021, **26**, 6501.

31 J. Yang, W. H. Li, S. Tan, K. Xu, Y. Wang, D. Wang and Y. Li, The Electronic Metal-Support Interaction Directing the Design of Single Atomic Site Catalysts: Achieving High Efficiency Towards Hydrogen Evolution, *Angew. Chem., Int. Ed.*, 2021, **60**, 19085–19091.

32 J. Lu, S. Zhang, H. Zhou, C. Huang, L. Xia, X. Liu, H. Luo and H. Wang, Ir Single Atoms and Clusters Supported on α-MoC as Catalysts for Efficient Hydrogenation of CO_2 to CO, *Wuli Huaxue Xuebao*, 2023, **39**, 2302021.

33 Y. Sun, N. Zhang, Y. Yue, J. Xiao, X. Huang and A. Ishag, Recent advances in the application of zeolitic imidazolate frameworks (ZIFs) in environmental remediation: a review, *Environ. Sci.: Nano*, 2022, **9**, 4069–4092.

34 S. Li, H. Wang, C. Qiu, J. Ren, Y. Peng, Y. Liu, F. Dong and Z. Bian, Electronic structure regulation of Fe single atom coordinated nitrogen doping MoS_2 catalyst enhances the Fenton-like reaction efficient for organic pollutant control, *J. Hazard. Mater.*, 2024, **467**, 133756.

35 J. Qiu, D. Wang, Y. Chang, Q. Feng, Z. Liu, M. Pang, D. Meng, Y. Feng and C. Fan, Anchoring single-atom Cu on tubular g-C_3N_4 with defect engineering for enhanced Fenton-like reactions to efficiently degrade carbamazepine: Performance and mechanism, *Chem. Eng. J.*, 2024, **479**, 147841.

36 Y. Luo and D. Wang, Enhancing Heterogeneous Catalysis by Electronic Property Regulation of Single Atom Catalysts, *Wuli Huaxue Xuebao*, 2023, **39**, 2212020.

37 W. Yang, L. Chen, Z. Jia, B. Zhou, Y. Liu, C. Wu and Z. Gao, Design of single-atom catalysts for NO oxidation using OH radicals, *J. Mater. Chem. A*, 2023, **11**, 23249–23259.

38 W. Yang, L. Li, M. Zhao, H. Huang, X. Ding, C. Wu, I. D. Gates and Z. Gao, Theoretical prediction of graphene-based single-atom iron as a novel catalyst for catalytic oxidation of Hg^0 by O_2, *Appl. Surf. Sci.*, 2020, **508**, 145035.

39 W. Yang, Z. Gao, X. Liu, X. Li, X. Ding and W. Yan, Single-atom iron catalyst with single-vacancy graphene-based substrate as a novel catalyst for NO oxidation: a theoretical study, *Catal. Sci. Technol.*, 2018, **8**, 4159–4168.

40 C. Ling, X. Liu, H. Li, X. Wang, H. Gu, K. Wei, M. Li, Y. Shi, H. Ben, G. Zhan, C. Liang, W. Shen, Y. Li, J. Zhao and L. Zhang, Atomic-Layered Cu5 Nanoclusters on FeS_2 with Dual Catalytic Sites for Efficient and Selective H_2O_2 Activation, *Angew. Chem., Int. Ed.*, 2022, **61**, e202200670.

41 Y. Mao, J. Cheng, H. Guo, L. Qian, J. Tu and W. Yang, Acid-base bifunctional Fe-NC catalyst with Fe-N4 and Fe nanoparticles active sites derived from Fe-doped ZIF-8 boosted microalgal lipid conversion, *Appl. Surf. Sci.*, 2023, **634**, 157679.

42 W. Yang, X. Liu, X. Chen, Y. Cao, S. Cui, L. Jiao, C. Wu, C. Chen, D. Fu, I. D. Gates, Z. Gao and H.-L. Jiang, A Sulfur-Tolerant MOF-Based Single-Atom Fe Catalyst for Efficient Oxidation of NO and Hg0, *Adv. Mater.*, 2022, **34**, 2110123.

43 C. Zhu, Y. Nie, S. Zhao, Z. Fan, F. Liu and A. Li, Constructing surface micro-electric fields on hollow single-atom cobalt catalyst for ultrafast and anti-interference advanced oxidation, *Appl. Catal., A*, 2022, **305**, 121057.

44 W. Zhu, S. Ndayiragije, X. Zuo, X. Zhang, G. Wang and X. Wang, ZIF-8-derived single-atom Cu and N co-coordinated porous carbon as bifunctional material for SMX removal, *J. Environ. Chem. Eng.*, 2022, **10**, 107758.

45 G. Kresse and J. Furthmüller, Efficiency of ab-initio total energy calculations for metals and semiconductors using a plane-wave basis set, *Comput. Mater. Sci.*, 1996, **6**, 15–50.

46 G. Kresse and J. Furthmüller, Efficient iterative schemes for ab initio total-energy calculations using a plane-wave basis set, *Phys. Rev. B: Condens. Matter Mater. Phys.*, 1996, **54**, 11169–11186.

47 J. P. Perdew, K. Burke and M. Ernzerhof, Generalized Gradient Approximation Made Simple, *Phys. Rev. Lett.*, 1996, **77**, 3865–3868.

48 G. Kresse and D. Joubert, From ultrasoft pseudopotentials to the projector augmented-wave method, *Phys. Rev. B: Condens. Matter Mater. Phys.*, 1999, **59**, 1758–1775.

49 L. Ma, J.-M. Zhang, K.-W. Xu and V. Ji, A first-principles study on gas sensing properties of graphene and Pd-doped graphene, *Appl. Surf. Sci.*, 2015, **343**, 121–127.

50 W. Yang, H. Huang, X. Liu, J. Ren, K. Ma, Z. Pan, Z. Ding, X. Ding and Z. Gao, Screening the activity of single-atom catalysts for the catalytic oxidation of sulfur dioxide with a kinetic activity model, *Chem. Commun.*, 2020, **56**, 11657–11660.

51 G. Henkelman, A. Arnaldsson and H. Jónsson, A fast and robust algorithm for Bader decomposition of charge density, *Comput. Mater. Sci.*, 2006, **36**, 354–360.

52 G. Henkelman, B. P. Uberuaga and H. Jónsson, A climbing image nudged elastic band method for finding saddle points and minimum energy paths, *J. Chem. Phys.*, 2000, **113**, 9901–9904.

53 G. Henkelman and H. Jónsson, Improved tangent estimate in the nudged elastic band method for finding minimum energy paths and saddle points, *J. Chem. Phys.*, 2000, **113**, 9978–9985.

54 W. Zhang, L. Wang, C. Hou, Z. Zhu, E. Lichtfouse, C. Trapalis and C. Wang, Combined effect of Cu0 and oxygen vacancies in Cu-based zeolites enables highly efficient photo-Fenton-like performance for water purification, *Environ. Sci.: Nano*, 2024, **11**, 2481–2493.

55 J. Wang and S. Wang, Reactive species in advanced oxidation processes: Formation, identification and reaction mechanism, *Chem. Eng. J.*, 2020, **401**, 126158.

56 X. Huang, J. Ding and Q. Zhong, Catalytic decomposition of H_2O_2 over Fe-based catalysts for simultaneous removal of NO_X and SO_2, *Appl. Surf. Sci.*, 2015, **326**, 66–72.

57 H.-l. Li, F.-q. Dong, L. Bian, T.-t. Huo, X.-c. He, F. Zheng, Z.-z. Lv, L.-m. Jiang and B. Li, Heterogeneous oxidation mechanism of SO_2 on γ-Al_2O_3 (110) catalyst by H_2O_2: A first-principle study, *Colloids Surf., A*, 2021, **611**, 125777.

58 Y. Sun, R. Yi, C. Hu and L. Lyu, Enhanced purification efficiency for pharmaceutical wastewater through a pollutant-mediated H_2O_2 activation pathway over CuZnS

nano-aggregated particles, *Environ. Sci.: Nano*, 2022, **9**, 4317–4324.

59 A. Cao and J. K. Nørskov, Spin Effects in Chemisorption and Catalysis, *ACS Catal.*, 2023, **13**, 3456–3462.